

The spectrum of a 1- μm -wavelength-driven tin microdroplet laser-produced plasma source in the 5.5–265.5 nm wavelength range

Z. Bouza,¹ J. Byers,² J. Scheers,^{1,3} R. Schupp,¹ Y. Mostafa,¹ L. Behnke,¹ Z. Mazzotta,¹ J. Sheil,¹ W. Ubachs,^{1,3} R. Hoekstra,^{1,4} M. Bayraktar,² and O. O. Versolato^{1,3, a)}

¹⁾Advanced Research Center for Nanolithography, Science Park 106, 1098 XG Amsterdam, The Netherlands

²⁾Industrial Focus Group XUV Optics, MESA+ Institute for Nanotechnology, University of Twente, Drienerlolaan 5, 7522 NB Enschede, The Netherlands

³⁾Department of Physics and Astronomy, and LaserLaB, Vrije Universiteit, De Boelelaan 1081, 1081 HV Amsterdam, The Netherlands

⁴⁾Zernike Institute for Advanced Materials, University of Groningen, Nijenborgh 4, 9747 AG Groningen, The Netherlands

(Dated: 24 October 2021)

We present a calibrated spectrum in the 5.5–265.5 nm range from a microdroplet-tin Nd:YAG-laser-produced plasma under conditions relevant for the production of extreme ultraviolet light at 13.5 nm for nanolithography. The plasma emission spectrum, obtained using a custom-built transmission-grating spectrometer, results from a careful calibration of a series of filters enabling measurements free of any higher diffraction orders. Specifically, Zr, Si and Al thin-foil filters, and bulk LiF, MgF₂ and UV fused silica filters are employed. A further filter using four SiC mirrors is used to record the otherwise inaccessible 40–100 nm range. The resulting corrected and concatenated spectra are shown to accurately match in their respective overlap regions. The possibility to measure spectra over this broad range enables the optimization of current and future sources of EUV light for nanolithography by providing the diagnostics required for minimizing the emission of unwanted wavelength bands.

I. INTRODUCTION

Laser-produced plasma (LPP) generated from liquid tin (Sn) microdroplets provides extreme ultraviolet (EUV) light for modern nanolithography^{1–7}, enabling the continued reduction of feature sizes on affordable integrated circuits (ICs). Such laser-produced plasmas of tin are characterized by a strong emission peak near 13.5 nm, originating from transitions between complex excited states in multiply charged Sn¹⁰⁺–Sn¹⁵⁺ ions^{8–17}.

Multilayer optics are used in industrial lithography machines to collect the EUV light from its source, and to provide an image of the so-called mask onto the wafer. These optics are designed to reflect wavelengths in a 2% wavelength bandwidth centered around 13.5 nm (the bandwidth limitation is in part due to the many, ~ 10 required reflective surfaces)^{18,19}. As such, most spectroscopic works on Sn LPPs have focused on the “in-band” wavelength region^{17,20–24}, or on nearby out-of-band (OOB) EUV emission features^{14,23,25–31}, spectral regions which may help diagnose the plasma in terms of its main in-band emitters’ charge states or temperature. Little spectroscopic information is available for longer, vacuum (VUV)- and deep-ultraviolet (DUV) wavelengths in particular in terms of relative (or absolute) emission intensities. Available spectra in the literature either show vacuum- or deep-ultraviolet spectra without the EUV region around 13.5 nm^{32–36}, or if the EUV region is presented, the spectral range between EUV and DUV is not

shown^{37–42}.

VUV/DUV emission may be transported through the multilayer optics systems and expose the wafer. Given the significant photon energy, this exposure may influence the chemical processes on the wafer and negatively impact imaging contrast and quality^{43,44}. As such, it is of significant interest to understand in detail the spectrum of EUV generating LPPs in terms of their absolute emission intensity. This will enable identifying the origins of many yet-unknown emission features and enable the development of mitigation strategies, i.e. minimize the OOB emission. In particular, the wavelength range of 30–90 nm is important for EUV lithography due to the strong absorption by hydrogen which is present as a buffer gas in the EUV source chambers. Photoionization of hydrogen molecules by DUV radiation generates plasmas in the scanner which can degrade important optical components⁴⁵. It is challenging to obtain the source spectrum in this wavelength range due to strong contributions from higher diffraction orders of the very strong emission feature centered around 13.5 nm.

We present an intensity-calibrated spectrum of a droplet-based tin plasma driven by 1- μm laser light in the wavelength range between 5.5–265.5 nm. A custom-built transmission grating spectrometer (TGS) is used to record the spectrum using a 1000 lines per mm grating. Higher diffraction orders, which would otherwise render impossible the detection of longer wavelengths, are eliminated by using Zr, Si, Al, LiF, MgF₂, and UV fused silica (UVFS) filters. An additional novel filter using four SiC mirrors is used to record the 40–100 nm region which would, given the dominant contribution from the higher diffraction orders of the EUV band if unfiltered, other-

^{a)}versolato@arcn1.nl

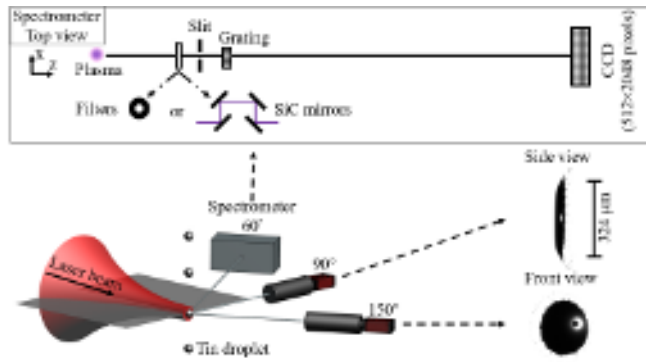


FIG. 1. Experimental setup showing the front- and side-view shadowgraphs of the tin targets used for plasma generation as recorded by two cameras. The upper, boxed figure is a schematic of the transmission grating spectrometer.

wise remain inaccessible. Careful calibration of these filters and the transmission grating combined with the response of the camera enables the absolute calibration of the full operating band and to obtain a spectrum free of any higher diffraction orders.

II. EXPERIMENTAL SETUP

In our experiments, molten tin microdroplets of $46\ \mu\text{m}$ diameter are first irradiated by a relatively low intensity ($\sim 10^9\ \text{W}/\text{cm}^2$), $1\text{-}\mu\text{m}$ wavelength pre-pulse (PP) from an Nd:YAG laser⁴⁶. The microdroplets are dispensed from a droplet generator inside a vacuum vessel with a background pressure of approximately 10^{-6} mbar. The beam profile of the PP laser is Gaussian of with a spatial full width at half maximum (FWHM) of $97\ \mu\text{m}$. The temporal profile is a Gaussian with a FWHM of 29 ns. For the presented experiments a constant PP energy of 6.8 mJ was used. The PP deforms the droplets into thin sheet targets which are radially symmetric and thickest in their center^{47–51}. The target diameter is controlled via a time delay between the pre- and main pulses, and for our experiments the time delay is set to 2000 ns, leading to a target diameter of $\sim 320\ \mu\text{m}$.

After the PP, the targets are irradiated with a high-intensity $1\text{-}\mu\text{m}$ -wavelength main pulse (MP) from a Nd:YAG laser. The pulse duration of the MP is 10 ns and the focal spot has a Gaussian beam profile with a FWHM of $103\ \mu\text{m}$. For the presented experiments, a fixed laser intensity of $2.3 \times 10^{11}\ \text{W}/\text{cm}^2$ was employed using a pulse energy of 293 mJ. The intensity was calculated as described in Ref. 27. Additional details regarding the droplet-based experimental setup can be found in Ref. 47. Finally, a simplified scheme of the experimental setup is presented in Fig. 1.

The spectral emission from the Sn laser-produced plasma is recorded using a broadband transmission grating spectrometer^{52,53} which is placed under an angle of 60° with respect to the incoming laser light. The different

| Filter material | Filter type | Thickness | Short wavelength cut-off (nm) |
|------------------|-------------|-----------|-------------------------------|
| Zr | Foil | 200 nm | 6.1 |
| Si | Foil | 200 nm | 12.5 |
| Al | Foil | 200 nm | 17 |
| SiC | Mirrors | 1 mm | 55 |
| LiF | Window | 2 mm | 129 |
| MgF ₂ | Window | 2 mm | <115* |
| UVFS | Window | 2 mm | 165 |

TABLE 1. Filters used in the spectral measurements with the transmission grating spectrometer. All short wavelength cut-offs are specified at 50% of the maximum transmission shown in the figures. * At 115 nm the transmission is $\sim 53\%$ of the maximum.

elements in the TGS are shown schematically in Fig. 1. The spectrometer is operated with a slit width of $50\ \mu\text{m}$ and a 1000 lines/mm transmission grating, achieving a FWHM instrument resolution of $0.8\ \text{nm}$ at $13.5\ \text{nm}$ ⁵². The use of the 1000 lines/mm transmission grating allows one to record emission in the $5.5\text{--}265.5\ \text{nm}$ wavelength region. The limits to this specific $5.5\text{--}265.5\ \text{nm}$ range are set on the short wavelength side by the onset ($> 5.5\ \text{nm}$) of the availability of calibration data for the diffraction grating (see Section III B). On the long wavelength side, the limit ($< 265.5\ \text{nm}$) is due to the geometry of the spectrometer. Furthermore, the spectrometer contains Zr, Si, Al, LiF, MgF₂, UVFS as well as SiC mirrors as tabulated in Table 1. The Zr, Si, and Al filters are foil filters with a common thickness of 200 nm. The foils are supported with a Ni mesh with 10 lines/inch period. The SiC system comprises four bulk-SiC mirrors which are placed under an angle of 45° with respect to the optical axis (see Fig. 1). The transmission grating, the filters Zr, Si, Al and the SiC mirrors are calibrated at the beamline facilities of the Physikalisch-Technische Bundesanstalt (PTB), at the BESSY-II synchrotron, Berlin, limited to wavelengths $> 5.5\ \text{nm}$. The LiF, MgF₂ and UVFS filters are calibrated for wavelengths down to 115 nm using a vacuum-ultraviolet spectrograph equipped with a deuterium lamp.

The diffracted light in the TGS is recorded on a back-illuminated charge-coupled device (CCD) from Greteyes GmbH (GE2048 512BI UV1). The CCD is cooled to -30°C to reduce thermal noise. Background images are then subtracted from the recorded spectra to eliminate the dark counts as well as read-out noise. The resulting CCD images are cropped and corrected for shear and tilt that may be introduced by a misalignment of the slit and the grating with respect to the CCD pixel array. Next, the pixel counts are averaged along the non-dispersive axis and corrected for the respective exposure times. The resulting spectra are then corrected for filter efficiency,

the first-order diffraction efficiency of the grating, the camera response and the solid angle of the spectrometer. The spectrometer has a solid angle of 37×10^{-11} sr that is calculated using the slit width, pixel size and the distance to the plasma.

For the wavelength calibration, a measurement with the Al filter is used. The sharp filter edge at 17.056 nm^{54} and its higher orders enable accurate calibration of the wavelength axis. Here, the higher diffraction orders are advantageous - for wavelength calibration.

III. RESULTS

In this section, three necessary types of corrections are applied to the raw spectra, namely the (A) filter transmission; (B) grating diffraction efficiency; and (C) CCD response.

A. Filter transmission

Spectra were recorded in the 5.5–265.5 nm wavelength region using different filters. The advantage of capturing spectra using different filters is that each filter allows for the measurement of different wavelength regions clear from higher order contributions. In the following, we sub-divide our discussion of the 5.5–265.5 nm spectra into three regions: (1) 5.5–40 nm, (2) 40–115 nm and (3) 115–265.5 nm, and we discuss each region individually.

1. 5.5–40 nm wavelength range

For the investigation of the 5.5–40 nm wavelength range we recorded four sets of spectra using (i) no filter and the filters (ii) Zr, (iii) Si, and (iv) Al. The measured spectra are presented in Fig. 2(a).

The Zr filter has a cut-off at $\sim 6.1 \text{ nm}$ which allows for recording a higher-order-free tin LPP spectrum in the ~ 6.1 – 12.2 nm region. The Si filter exhibits a cut-off at $\sim 12.5 \text{ nm}$ so in that way the spectrum is pure in the range of ~ 12.5 – 25 nm . The Al filter has the advantage of a longer wavelength cut-off at $\sim 17 \text{ nm}$ such that all orders of the strong 13.5 nm emission feature are absent and a clean measurement in the range ~ 17 – 34 nm is possible.

The transmission functions of the various filters are tabulated in the CXRO database⁵⁴, however such transmission data is only valid for pristine samples. These filters typically suffer from oxidation and are subject to contamination from hydrocarbons and tin deposition. To obtain reliable transmission functions, the filters are calibrated at the PTB in Berlin. The calibration results are shown in Fig. 2(b), (c) and (d). The calibration procedure comprises two steps. First, for each filter type, the entire filter area was sampled at a single wavelength (13.5 nm for the Al filter, 17.5 nm for the Si and Zr filters) using a $0.5 \times 0.5 \text{ mm}^2$ beam, enabling to obtain a detailed

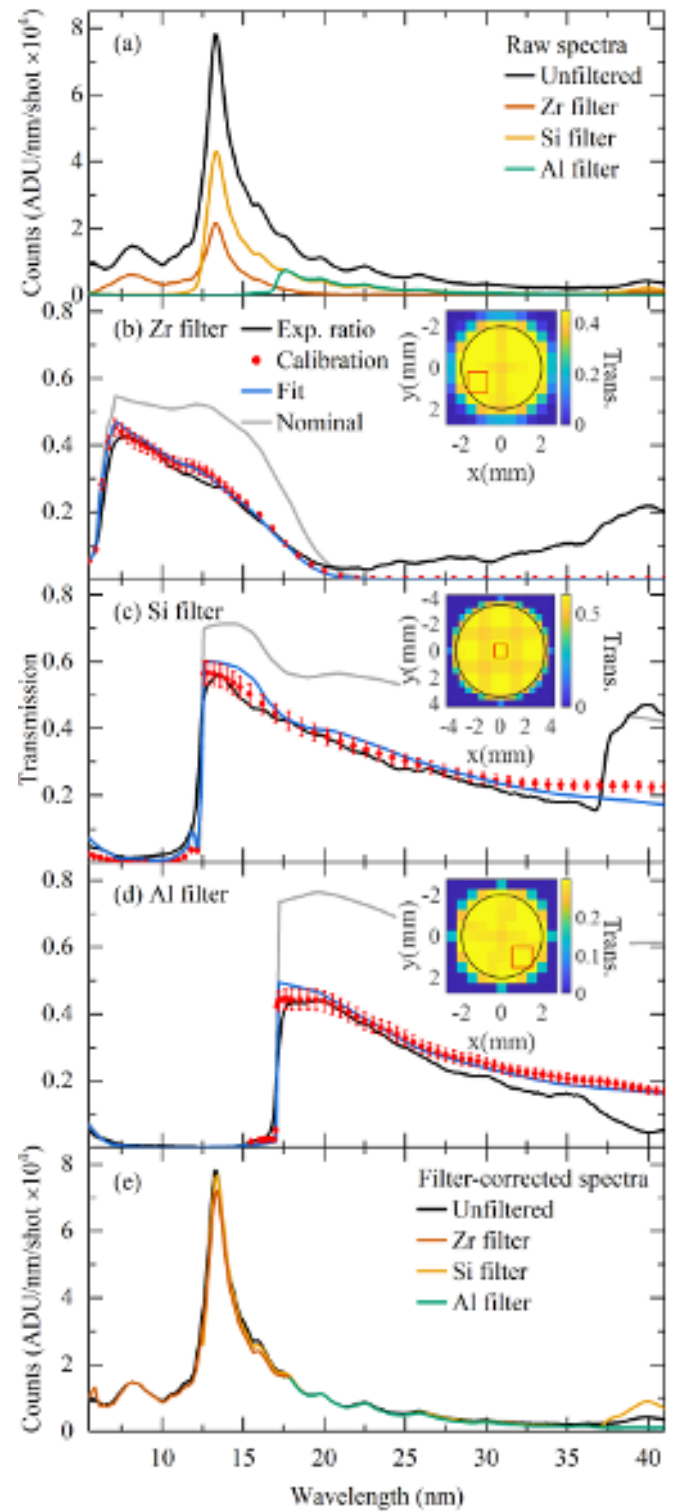


FIG. 2. (a) Raw emission spectra obtained from tin LPP using Zr, Si, and Al filters, as well as using no filter. ADU: arithmetic digital unit. Filter transmissions for (b) Zr, (c) Si and (d) Al filters. The experimental ratio is the result of the division of the respective filtered by the unfiltered spectra; the calibration is from PTB; and the fitted curve is obtained taking oxidation into account, while the nominal one is the transmission obtained CXRO. Insets: Transmission maps measured at 13.5 nm for Zr and Si, and at 17.5 nm for Al. Red squares depict the location of the filter used for the wavelength scan. (e) Spectra corrected for the respective filter transmission functions.

“map” of the transmission. Second, at one particular position on the filter (indicated by red squares in the inset figures), the full wavelength range is measured. The recorded transmission function was subsequently scaled by a factor proportional to the average transmission at the wavelength of the first measurement step (within the filter window indicated by the black circle in the inset figures). The error bars on this scaled transmission curve (red data points in Fig. 2(b), (c) and (d)) represent one standard deviation from the average across the filter.

Superimposed in black in the same figures are experimental estimates of the transmission function. These estimates are obtained by dividing the respective filtered spectra by the unfiltered spectra. These ratios may serve only as estimates as they are influenced by higher diffraction orders.

In all cases, the filter transmission is significantly lower than theoretical transmission that would be obtained from the CXRO database using the nominal thickness (shown as light gray lines). In an attempt to quantitatively explain the differences between the calibration and nominal CXRO database entries, we simulate the influence of finite oxidation of the filter surfaces using the following equation (Al as an example):

$$T = \exp(-n_{Al}\mu_{Al}d_{Al}) \times \exp(-n_{Al_2O_3}\mu_{Al_2O_3}d_{Al_2O_3}) \quad (1)$$

The symbols n , μ and d represent the number of atoms per unit volume, atomic photo-absorption cross section and thickness of the material, respectively. Thin film interference effects are verified to be negligible. We also accounted for the thickness of the non-oxidized part of the filter and the fraction of the filter material in the oxide layer sums up to the nominal thickness. The fraction of the filter material in the oxide layer is calculated by considering the atomic weights of the pure filter material and the oxidized filter material. For Al this fraction is calculated as $W_{Al}/W_{Al_2O_3}$, where W is the atomic/molecular weight. This consideration allows fitting the $T(\lambda)$ function to the PTB measured transmission curve with a single free fit parameter, namely the thickness of the oxide layer. The fit results shown in Fig. 2 are in good agreement with the calibration data. The obtained oxide thicknesses range from 17 nm in the Al filter case to 49 nm in the Zr filter case. We find optimum agreement between the simulated and experimentally-determined calibration curves for oxide layer thickness of 49 nm ZrO_2 layer (with 169 nm pure Zr remaining), 19 nm SiO_2 (192 pure Si) and 17 nm Al_2O_3 (193 nm pure Al). The substantial oxide layers (we assume the oxide layer is divided between front and back sides of the filter) are in fact in agreement with the expected oxide layer thickness of such metal foils. More specifically, it has been shown in Ref. 55 using Auger depth profiling, a 100 nm thick Zr filter can have 10 nm thick oxide layers on both sides of the filter. The total oxide layer thickness in Ref. 55 is of the same order of magnitude as the oxide layer thickness we have found. The same study⁵⁵ further shows that carbon and carbide mixed with Zr is also present throughout the fil-

ter, decreasing the transmission further. Since carbon and carbide mixing is not taken into account in our analysis, our calculations may overestimate the ZrO_2 layer thickness. For the Si filter, a total oxide layer thickness of 66 nm has been reported, somewhat thicker than what we found⁵⁶. For the Al filter, oxide thicknesses around 15 nm have been reported, which matches well with 17 nm thickness that is found here^{56,57}. All in all, the PTB-calibrated transmission curves can be well understood from our model assuming a relatively thick oxide layer coating the pure filter surfaces.

Next, the spectra are corrected with the filter transmission data from PTB, the results of which are shown Fig. 2(e). The corrected spectra are shown starting from the short wavelength cut-off of each filter onward till the calibrated transmission drops below 10%. The corrected spectra are in very good agreement with each other (cf. Fig. 2 (e)). The dominant remaining difference is visible at 40 nm wavelength and can be attributed to the third-order contribution of the main emission feature at 13.5 nm that here only impacts the unfiltered spectrum and the Si filtered spectrum (the Zr-filtered spectrum is shown up to 18 nm where the transmission drops below 10%). The Al-filtered spectrum is free of this third-order diffraction feature and will be used for this wavelength range.

2. 40–115 nm wavelength range

For the investigation of the 40–115 nm wavelength range we use the SiC mirrors. In Fig. 3(a), the spectrum obtained using the SiC mirrors is presented. In the same figure a scaled unfiltered spectrum is also presented for comparison. The peak in the unfiltered spectrum in the 65–70 nm range can be attributed to the fifth diffraction order of the dominant 13.5 nm emission feature. The spectral intensities in the SiC mirrors measurements are between two and three orders of magnitude lower than the unfiltered spectrum.

The SiC mirrors were sent to PTB for calibration in order to measure its total reflection efficiency. The resulting calibration is compared to the theoretical response curve in Fig. 3(b). The difference can be attributed partially to contamination but also to scattering due to roughness.

The LPP spectrum is then corrected with the reflectivity calibration data from PTB, the results of which are shown in Fig. 3(c). The unfiltered and SiC filtered spectra show significant differences, highlighting the important contribution from higher orders to the spectrum and emphasizing the need for suppression of higher orders using filters as is done here.

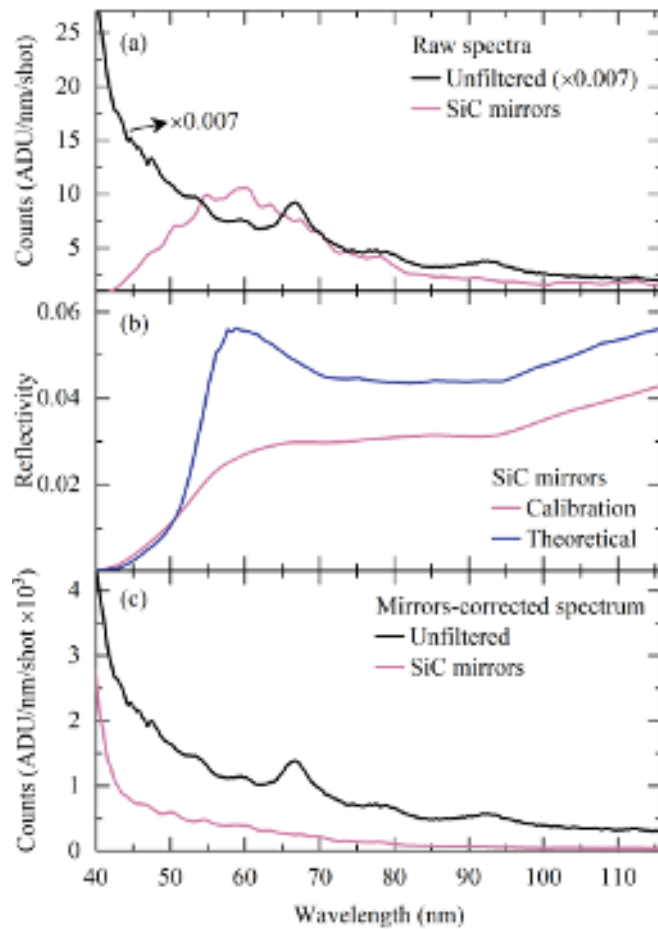


FIG. 3. (a) Raw tin LPP emission spectra using the SiC mirrors as well as no filter. The unfiltered spectrum is multiplied by $\times 0.007$ for better visibility. (b) SiC mirrors reflectivity curves: one calibrated by PTB and one from theory (see main text). (c) Unfiltered spectrum and spectrum corrected for the SiC mirrors reflectivity.

3. 115–265.5 nm wavelength range

To investigate the 115–265.5 nm wavelength range we have recorded spectra using (i) no filter and the filters (ii) LiF, (iii) MgF_2 , and (iv) UVFS. The spectra are shown Fig. 4(a). The spectrum with the LiF filter extends smoothly below 115 nm but the spectrum recorded using the MgF_2 filter exhibits a steep decrease. The UVFS filter has the longest cut-off wavelength at 165 nm. All filters transmit at wavelengths above 265.5 nm which is the limit of the measurement range, set by the spectrometer.

In Fig. 4(b), the calibrated transmission efficiency curves of the three filters used for this wavelength region are presented. Since the upper limit of the wavelength axis of our recorded spectra is ~ 265.5 nm, a combination of two of the filters (either LiF or MgF_2 with UVFS) in the 115–265.5 nm range will fully suppress all higher order contributions.

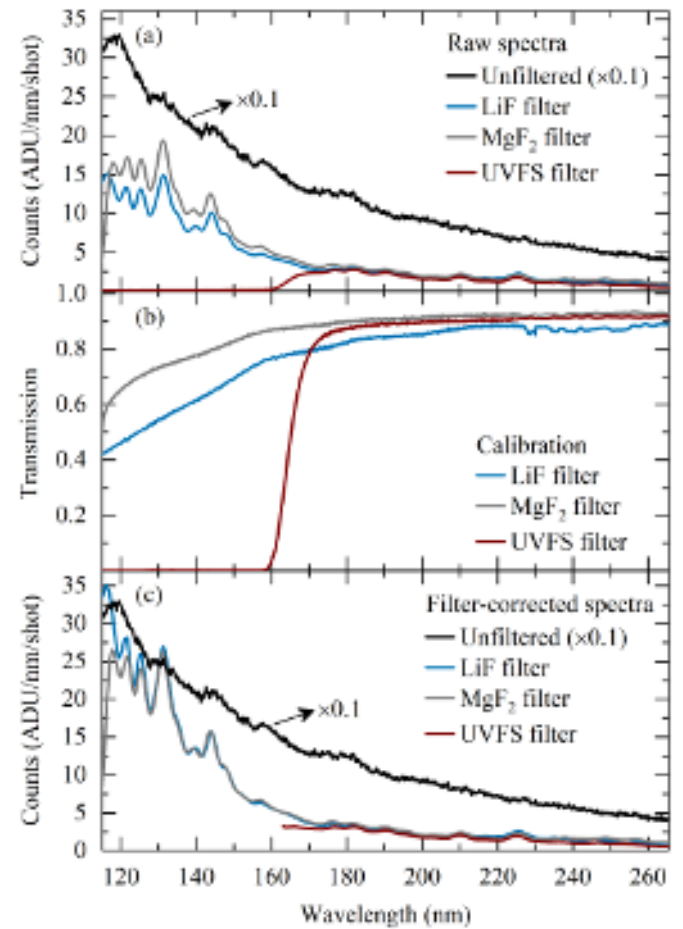


FIG. 4. (a) Raw emission spectra from a tin LPP using the LiF, MgF_2 and UVFS filter as well as no filter. The unfiltered spectrum is multiplied by $\times 0.1$ for better visibility. (b) Filter transmission curves for the various filters. (c) Spectra corrected for the respective filter transmission functions.

We present the filter-corrected spectra in Fig. 4(c). The three filter-corrected spectra are generally in good agreement with each other. The most significant difference, occurring below 120 nm, is related to the accuracy of the onset of the transmission of the MgF_2 filter and the precision of the relative wavelength calibration of the experiments and calibration. The comparison between the unfiltered spectrum to the filter-corrected spectra highlights the prominent contribution from high diffraction orders. The apparent intensity, i.e., counts, of the unfiltered spectrum is more than an order of magnitude stronger than the true signal, thus emphasizing the need to use filters.

In Fig. 5 we present the full spectrum in the 5.5–265.5 nm wavelength range obtained from concatenating the filtered spectra using only their respective ranges free of any higher diffraction orders. The individual y-axis values are shown to accurately “connect” at the respective overlap regions. We note that no free fit factors have been used to obtain this match. Instead, it is the accurate

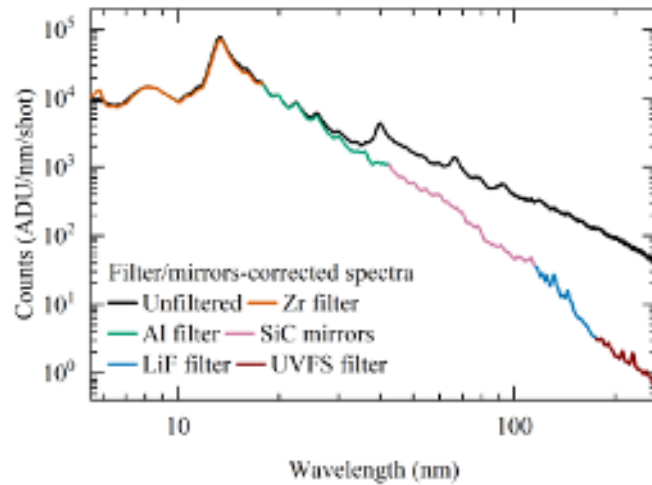


FIG. 5. Concatenated spectra from tin LPP using the various filters, corrected for the respective transmission functions (see main text). The chosen range for each spectrum is free of any higher diffraction orders. The unfiltered spectrum is also shown for comparison.

calibration of the filter transmissions that enables this good agreement. As seen before, strong contributions from higher diffraction orders are visible. In particular the odd multiples of the main 13.5 nm emission feature stand out, starting from the third diffraction order.

B. Grating diffraction efficiency

The first-order diffraction efficiency of the grating is shown in Fig. 6(a), as obtained from calibration at PTB. The feature that stands out is the “kink” near 12 nm that originates from the Si L-edge absorption in Si_3N_4 material present in the transmission grating⁵².

C. CCD response

The CCD camera response is a product of three components: the gain, quantum yield (QY) and quantum efficiency (QE)⁶⁰. The gain relates the ADU to the generated electrons and has the units of ADU/e^- . For the camera that is used in this experiment, the camera gain is specified by the manufacturer⁵⁸ as $0.83 \text{ ADU}/e^-$.

The QY is defined as the number of electrons generated per detected photon, and is proportional to the energy of the photon. A typical assumption in the EUV and VUV wavelength ranges^{59,61} is that a photon energy of 3.66 eV, which corresponds to the indirect bandgap of Si, is needed to generate an electron. A detected photon of energy E would thus generate $E/(3.66 \text{ eV})$ electrons. As pointed out also by Heymes *et al.*⁶¹ this assumption breaks down in the optical range where QY will instead converge to a value of one (1). In the here stud-

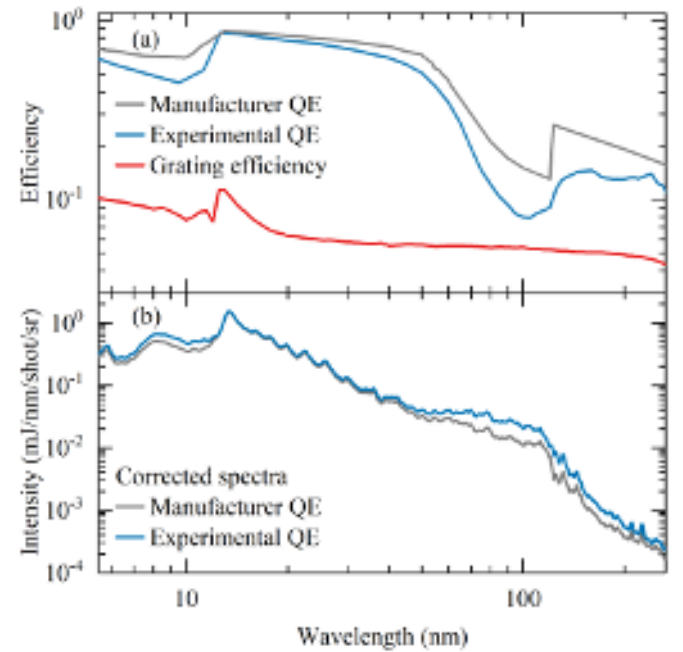


FIG. 6. (a) Grating efficiency for the first diffraction order and QE of the CCD camera, comparing manufacturer QE⁵⁸ or experimental QE⁵⁹ data (see main text). (b) Concatenated spectra (cf. Fig. 5) after correcting for the diffraction efficiency of the grating, the CCD response using either manufacturer or experimental QE data and solid angle.

ied wavelength range, however, the simple $1/3.66 \text{ e}^-/\text{eV}$ rule is in good agreement with a more detailed treatment^{59,60}. Correcting for QY enables converting the number of electrons to the number of detected photons, or to the amount of detected energy in units of eV with a proportionality constant of 3.66. Hence, the QY for the wavelength range explored in this work can be written in units of e^-/eV or e^-/mJ as $\text{QY} = 1/3.66 \text{ e}^-/\text{eV} = 1.71 \times 10^{15} \text{ e}^-/\text{mJ}$.

The QE is defined as the ratio of the number of detected photons to the number of photons arriving on the detector surface. Hence, it is also equal to the ratio of detected to incident energy. In Fig. 6(a) we show two such quantum efficiency curves. The first is obtained from the manufacturer of the CCD used in our experiments⁵⁸. We note however that the calibration provided by the manufacturer depends, in part, on simulations and not experiments⁶². According to their simulations, the sharp edge around 120 nm originates from thin film interference, assuming a sharp interface between the assumed SiO_2 layer and the active Si CCD surface. In reality, the boundary is expected to be less sharp due to intermixing. As a result, the QE curve is expected to have a smoother shape. In search of experimental support for our QE calibration we employ the recent results⁵⁹. Further experimental QE studies are found in previous works^{62–64}. Comparing the two QE curves in Fig. 6(a) we note that there is a striking difference near 120 nm where a sharp,

| Wavelength range (nm) | Corresponding filter | Energy (mJ/shot/sr) | (%) of total energy |
|-----------------------|----------------------|---------------------|---------------------|
| 5.5–17.5 | Zr | 7.1 | 54.7 |
| (13.5 nm $\pm 1\%$ *) | (Zr) | (0.4) | (3.1) |
| 17.5–42.5 | Al | 4.2 | 32.5 |
| 42.5–115 | SiC | 1.5 | 11.4 |
| 115–175.5 | LiF | 0.2 | 1.2 |
| 175.5–265.5 | UVFS | 0.03 | 0.2 |
| Total energy | | 13.0 | |

TABLE 2. Energy emitted towards the spectrometer, i.e. under a 60° angle cf. Fig. 1, in the various wavelength ranges using manufacturer QE data cf. Fig. 6. *The value for the energy emitted in the 2%-wavelength bandwidth centered around 13.5 nm is impacted on by the limited resolution of the spectrometer (0.8 nm at 13.5 nm).

steep edge is visible in the QE from the manufacturer which is not supported (either in amplitude or shape) by recent experimental work⁵⁹. The differences between the available QE curves may be due to dissimilarities in manufacturing processes or, for instance, to possible aging effects. Considering the significant differences, the overall uncertainty in our final spectrum is expected to be dominated by the QE curve.

As the final step, the concatenated spectra of Fig. 5 are corrected for the camera response (gain, QY, and QE) together with the solid angle of the spectrometer (37×10^{-11} sr) and the resulting corrected full-range spectrum is shown in Fig. 6(b). Integral energies emitted in the various wavelength ranges, following the filters used, are presented in Table 2. The final corrections, using either QE curve, produce a “knee” near 120 nm wavelength that is not visible in the concatenated data of Fig. 5 which may point at a discrepancy between the true QE and the available QE curves.

Further corrections for the source size (possibly weakly wavelength-dependent) and for the precise time dependence of the transient emission are required to interpret the obtained intensity in terms of spectral radiance. These steps are left as future work but may be expected to have only limited impact on the overall shape of the emission spectrum as shown in Fig. 6(b). Nevertheless, the obtained spectrum enables diagnosing the energy distribution of the LPP that is useful for optimizing the LPP based EUV sources.

IV. CONCLUSIONS

We present a fully calibrated spectrum in the 5.5–265.5 nm range from a microdroplet-tin Nd:YAG-laser-produced plasma. The spectrum, obtained using a transmission grating spectrometer, is the result of a careful cal-

ibration of a series of filters enabling measurements free of any higher diffraction orders. Specifically, we use Zr, Si, Al foil filters and bulk LiF, MgF₂, and UVFS filters. A further filter using four SiC mirrors is used to record the otherwise inaccessible 40–100 nm region. The photon energy in this particular wavelength range is significant and provides input for further studies on the impact of EUV-induced-plasma in the EUV source vessel. The fully corrected and concatenated spectra are shown to accurately match in their respective overlap regions demonstrating the accuracy of the calibration procedure. The dominant remaining uncertainty stems from the correction for quantum efficiency. Our calibration enables the optimization of current and future sources of EUV light for nanolithography by providing metrology for minimizing the emission of unwanted wavelength bands that may limit imaging contrast or even impact machine uptime.

SUPPLEMENTARY MATERIAL

See supplementary material for the data presented in Figs. 5 and 6(b).

ACKNOWLEDGMENTS

Part of this work has been carried out within the Advanced Research Center for Nanolithography, a public-private partnership of the University of Amsterdam, the Vrije Universiteit Amsterdam, the Dutch Research Council (NWO) and the semiconductor equipment manufacturer ASML and was financed by Toeslag voor Topconsortia voor Kennis en Innovatie from the Dutch Ministry of Economic Affairs. The transmission grating spectrometer was developed in the Industrial Focus Group XUV Optics at the University of Twente and supported by the FOM Valorisation Prize 2011 awarded to F. Bijkerk and NanoNextNL Valorization Grant awarded to M. Bayraktar in 2015. This project is funded by TKI-HTSM with the project name “Spectral Unraveling of EUV Lithography Light Sources (SUN)”. This project received further funding from the European Research Council Starting Grant No. 802648 and is part of the VIDI research programme with Project No. 15697, which is financed by NWO. The authors would like to thank Dr. Julian Heymes (The Open University, Milton Keynes, UK) for his valuable contribution to this manuscript.

DATA AVAILABILITY

The data that support the findings of this study are available from the corresponding author upon reasonable request. The particular data that supports the findings of this study as presented in Figs. 5 and 6(b) are available within the article [and its supplementary material].

- ¹O. O. Versolato, "Physics of laser-driven tin plasma sources of EUV radiation for nanolithography," *Plasma Sources Sci. Technol.* **28**, 083001 (2019).
- ²M. Purvis, I. V. Fomenkov, A. A. Schafgans, M. Vargas, S. Rich, Y. Tao, S. I. Rokitski, M. Mulder, E. Buurman, M. Kats, J. Stewart, A. D. LaForge, C. Rajyaguru, G. Vaschenko, A. I. Ershov, R. J. Rafac, M. Abraham, D. C. Brandt, and D. J. Brown, "Industrialization of a robust EUV source for high-volume manufacturing and power scaling beyond 250 W," in *Extreme Ultraviolet (EUV) Lithography IX*, Vol. 10583, edited by K. A. Goldberg, International Society for Optics and Photonics (SPIE, 2018) pp. 476 – 485.
- ³S. K. Moore, "EUV lithography finally ready for fabs," *IEEE Spectr.* **55**, 46–48 (2018).
- ⁴H. Mizoguchi, H. Nakarai, T. Abe, K. M. Nowak, Y. Kawasuji, H. Tanaka, Y. Watanabe, T. Hori, T. Kodama, Y. Shiraishi, T. Yanagida, G. Soumagne, T. Yamada, T. Yamazaki, and T. Saitou, "High power LPP-EUV source with long collector mirror lifetime for high volume semiconductor manufacturing," in *2018 China Semiconductor Technology International Conference (CSTIC)* (2018) pp. 1–7.
- ⁵A. Y. Vinokhodov, M. S. Krivokorytov, Y. V. Sidelnikov, V. M. Krivtsun, V. V. Medvedev, and K. N. Koshelev, "Droplet-based, high-brightness extreme ultraviolet laser plasma source for metrology," *J. Appl. Phys.* **120**, 163304 (2016).
- ⁶V. Y. Banine, K. N. Koshelev, and G. H. P. M. Swinkels, "Physical processes in EUV sources for microlithography," *J. Phys. D: Appl. Phys.* **44**, 253001 (2011).
- ⁷J. Benschop, V. Y. Banine, S. Lok, and E. Loopstra, "Extreme ultraviolet lithography: Status and prospects," *J. Vac. Sci. Technol. B* **26**, 2204–2207 (2008).
- ⁸V. I. Azarov and Y. N. Joshi, "Analysis of the $4d^7-4d^65p$ transition array of the eighth spectrum of tin: Sn VIII," *J. Phys. B: At. Mol. Opt. Phys.* **26**, 3495–3514 (1993).
- ⁹S. S. Churilov and A. N. Ryabtsev, "Analysis of the $4p^6 4d^7-(4p^6 4d^64f + 4p^5 4d^8)$ transitions in the Sn VIII spectrum," *Opt. Spectrosc.* **100**, 660–666 (2006).
- ¹⁰S. S. Churilov and A. N. Ryabtsev, "Analyses of the Sn IX–Sn XII spectra in the EUV region," *Phys. Scr.* **73**, 614 (2006).
- ¹¹A. N. Ryabtsev, É. Y. Kononov, and S. S. Churilov, "Spectra of rubidium-like Pd X–Sn XIV ions," *Opt. Spectrosc.* **105**, 844–850 (2008).
- ¹²I. Y. Tolstikhina, S. S. Churilov, A. N. Ryabtsev, and K. N. Koshelev, "Atomic tin data," in *EUV sources for lithography*, edited by V. Bakshi (SPIE Press, 2006) Chap. 4, pp. 113–148.
- ¹³R. D'Arcy, H. Ohashi, S. Suda, H. Tanuma, S. Fujioka, H. Nishimura, K. Nishihara, C. Suzuki, T. Kato, F. Koike, J. White, and G. O'Sullivan, "Transitions and the effects of configuration interaction in the spectra of Sn XV–Sn XVIII," *Phys. Rev. A* **79**, 042509 (2009).
- ¹⁴H. Ohashi, S. Suda, H. Tanuma, S. Fujioka, H. Nishimura, A. Sasaki, and K. Nishihara, "EUV emission spectra in collisions of multiply charged Sn ions with He and Xe," *J. Phys. B: At. Mol. Opt. Phys.* **43**, 065204 (2010).
- ¹⁵J. Colgan, D. Kilcrease, J. Abdallah, M. Sherrill, C. Fontes, P. Hakel, and G. Armstrong, "Atomic structure considerations for the low-temperature opacity of Sn," *High Energy Density Phys.* **23**, 133–137 (2017).
- ¹⁶F. Torretti, A. Windberger, A. Ryabtsev, S. Dobrodey, H. Bekker, W. Ubachs, R. Hoekstra, E. V. Kahl, J. C. Berengut, J. R. Crespo López-Urrutia, and O. O. Versolato, "Optical spectroscopy of complex open- $4d$ -shell ions Sn^{7+} – Sn^{10+} ," *Phys. Rev. A* **95**, 042503 (2017).
- ¹⁷J. Scheers, C. Shah, A. Ryabtsev, H. Bekker, F. Torretti, J. Sheil, D. A. Czapski, J. C. Berengut, W. Ubachs, J. R. C. López-Urrutia, R. Hoekstra, and O. O. Versolato, "EUV spectroscopy of highly charged Sn^{13+} – Sn^{15+} ions in an electron-beam ion trap," *Phys. Rev. A* **101**, 062511 (2020).
- ¹⁸S. Bajt, J. B. Alameda, T. W. Barbee, Jr., W. M. Clift, J. A. Folta, B. B. Kaufmann, and E. A. Spiller, "Improved reflectance and stability of Mo-Si multilayers," *Opt. Eng.* **41**, 1797–1804 (2002).
- ¹⁹Q. Huang, V. Medvedev, R. van de Kruijs, A. Yakshin, E. Louis, and F. Bijkerk, "Spectral tailoring of nanoscale EUV and soft x-ray multilayer optics," *Appl. Phys. Rev.* **4**, 011104 (2017).
- ²⁰G. O'Sullivan, B. Li, R. D'Arcy, P. Dunne, P. Hayden, D. Kilbane, T. McCormack, H. Ohashi, F. O'Reilly, P. Sheridan, *et al.*, "Spectroscopy of highly charged ions and its relevance to EUV and soft x-ray source development," *J. Phys. B: At. Mol. Opt. Phys.* **48**, 144025 (2015).
- ²¹F. Torretti, J. Sheil, R. Schupp, M. Basko, M. Bayraktar, R. Meijer, S. Witte, W. Ubachs, R. Hoekstra, O. Versolato, *et al.*, "Prominent radiative contributions from multiply-excited states in laser-produced tin plasma for nanolithography," *Nat. Commun.* **11**, 1–8 (2020).
- ²²S. S. Churilov and A. N. Ryabtsev, "Analysis of the spectra of In XII–XIV and Sn XIII–XV in the far-VUV region," *Opt. Spectr.* **101**, 169–178 (2006).
- ²³W. Svendsen and G. O'Sullivan, "Statistics and characteristics of XUV transition arrays from laser-produced plasmas of the elements tin through iodine," *Phys. Rev. A* **50**, 3710–3718 (1994).
- ²⁴S. S. Churilov, R. R. Kildiyarova, A. N. Ryabtsev, A. Kramida, and Y. N. Joshi, "Analysis of the $4d^9-4d^8(4f+6p)$ transition array of Sn VI," *Phys. Scr.* **50**, 463–468 (1994).
- ²⁵F. Torretti, R. Schupp, D. Kurilovich, A. Bayerle, J. Scheers, W. Ubachs, R. Hoekstra, and O. O. Versolato, "Short-wavelength out-of-band EUV emission from Sn laser-produced plasma," *J. Phys. B: At. Mol. Opt. Phys.* **51**, 045005 (2018).
- ²⁶F. Torretti, F. Liu, M. Bayraktar, J. Scheers, Z. Bouza, W. Ubachs, R. Hoekstra, and O. Versolato, "Spectral characterization of an industrial EUV light source for nanolithography," *J. Phys. D: Appl. Phys.* **53**, 055204 (2019).
- ²⁷R. Schupp, F. Torretti, R. Meijer, M. Bayraktar, J. Scheers, D. Kurilovich, A. Bayerle, K. Eikema, S. Witte, W. Ubachs, R. Hoekstra, and O. Versolato, "Efficient generation of extreme ultraviolet light from Nd:YAG-driven microdroplet-tin plasma," *Phys. Rev. Appl.* **12**, 014010 (2019).
- ²⁸R. Schupp, F. Torretti, R. A. Meijer, M. Bayraktar, J. Sheil, J. Scheers, D. Kurilovich, A. Bayerle, A. A. Schafgans, M. Purvis, K. S. E. Eikema, S. Witte, W. Ubachs, R. Hoekstra, and O. O. Versolato, "Radiation transport and scaling of optical depth in Nd:YAG laser-produced microdroplet-tin plasma," *Appl. Phys. Lett.* **115**, 124101 (2019).
- ²⁹Z. Bouza, J. Scheers, A. Ryabtsev, R. Schupp, L. Behnke, C. Shah, J. Sheil, M. Bayraktar, J. R. C. López-Urrutia, W. Ubachs, R. Hoekstra, and O. O. Versolato, "EUV spectroscopy of Sn^{5+} – Sn^{10+} ions in an electron beam ion trap and laser-produced plasmas," *J. Phys. B: At. Mol. Opt. Phys.* **53**, 195001 (2020).
- ³⁰R. Schupp, L. Behnke, J. Sheil, Z. Bouza, M. Bayraktar, W. Ubachs, R. Hoekstra, and O. O. Versolato, "Characterization of 1- and 2- μm -wavelength laser-produced microdroplet-tin plasma for generating extreme-ultraviolet light," *Phys. Rev. Res.* **3**, 013294 (2021).
- ³¹L. Behnke, R. Schupp, Z. Bouza, M. Bayraktar, Z. Mazzotta, R. Meijer, J. Sheil, S. Witte, W. Ubachs, R. Hoekstra, and O. O. Versolato, "Extreme ultraviolet light from a tin plasma driven by a 2- μm -wavelength laser," *Opt. Express* **29**, 4475–4487 (2021).
- ³²H. Sakaguchi, S. Fujioka, S. Namba, H. Tanuma, H. Ohashi, S. Suda, M. Shimomura, Y. Nakai, Y. Kimura, Y. Yasuda, H. Nishimura, T. Norimatsu, A. Sunahara, K. Nishihara, N. Miyanaga, Y. Izawa, and K. Mima, "Absolute evaluation of out-of-band radiation from laser-produced tin plasmas for extreme ultraviolet lithography," *Appl. Phys. Lett.* **92**, 111503 (2008).
- ³³S. Namba, S. Fujioka, H. Sakaguchi, H. Nishimura, Y. Yasuda, K. Nagai, N. Miyanaga, Y. Izawa, K. Mima, K. Sato, and K. Takiyama, "Characterization of out-of-band radiation and plasma parameters in laser-produced Sn plasmas for extreme ultraviolet lithography light sources," *J. Appl. Phys.* **104**, 013305 (2008).

- (2008).
- ³⁴N. Gambino, B. Rollinger, D. Hudgins, and R. S. Abhari, "Spectral emission properties of a laser-produced plasma light source in the sub-200 nm range for wafer inspection applications," *J. Micro/Nanolithogr. MEMS MOEMS* **14**, 1 – 7 (2015).
 - ³⁵N. Gambino, B. Rollinger, M. Brandstätter, and R. S. Abhari, "Vacuum ultraviolet spectral emission properties of Ga, In and Sn droplet-based laser produced plasmas," *Spectrochim. Acta B: At. Spectrosc.* **122**, 149–156 (2016).
 - ³⁶J. Scheers, R. Schupp, R. Meijer, W. Ubachs, R. Hoekstra, and O. O. Versolato, "Time- and space-resolved optical Stark spectroscopy in the afterglow of laser-produced tin-droplet plasma," *Phys. Rev. E* **102**, 013204 (2020).
 - ³⁷I. V. Fomenkov, D. C. Brandt, A. N. Bykanov, A. I. Ershov, W. N. Partlo, D. W. Myers, N. R. Böwering, G. O. Vaschenko, O. V. Khodykin, J. R. Hoffman, E. V. L., R. D. Simmons, J. A. Chavez, and C. P. Chrobak, "Laser-produced plasma source system development," in *Emerging Lithographic Technologies XI*, Vol. 6517, edited by M. J. Lercel, International Society for Optics and Photonics (SPIE, 2007) pp. 1021 – 1031.
 - ³⁸D. Campos, S. S. Harilal, and A. Hassanein, "The effect of laser wavelength on emission and particle dynamics of Sn plasma," *J. Appl. Phys.* **108**, 113305 (2010).
 - ³⁹N. Davydova, E. van Setten, R. de Kruif, B. Connolly, N. Fukugami, Y. Kodera, H. Morimoto, Y. Sakata, J. Kotani, S. Kondo, T. Imoto, H. Rolff, A. Ullrich, R. K. Jaganatharaja, A. Lammers, D. Oorschot, C.-W. Man, G. Schiffflers, and J. van Dijk, "Black border, mask 3D effects: covering challenges of EUV mask architecture for 22 nm node and beyond," in *30th European Mask and Lithography Conference*, Vol. 9231, edited by U. F. W. Behringer, International Society for Optics and Photonics (SPIE, 2014) pp. 1 – 14.
 - ⁴⁰H. Parchamy, J. Szilagyi, M. Masnavi, and M. Richardson, "Ultraviolet out-of-band radiation studies in laser tin plasma sources," *J. Appl. Phys.* **122**, 173303 (2017).
 - ⁴¹M. van de Kerkhof, F. Liu, M. Meeuwissen, X. Zhang, R. de Kruif, N. Davydova, G. Schiffflers, F. Wählich, E. van Setten, W. Varenkamp, K. Ricken, L. de Winter, J. McNamara, and M. Bayraktar, "Spectral purity performance of high-power EUV systems," in *Extreme Ultraviolet (EUV) Lithography XI*, Vol. 11323, edited by N. M. Felix and A. Lio, International Society for Optics and Photonics (SPIE, 2020) pp. 435 – 450.
 - ⁴²M. A. van de Kerkhof, F. Liu, M. Meeuwissen, X. Zhang, M. Bayraktar, R. C. de Kruif, and N. V. Davydova, "High-power EUV lithography: spectral purity and imaging performance," *J. Micro/Nanolithogr. MEMS MOEMS* **19**, 1 – 16 (2020).
 - ⁴³K. Liu, Y. Li, F. Zhang, and M. Fan, "Transient thermal and structural deformation and its impact on optical performance of projection optics for extreme ultraviolet lithography," *Jpn. J. Appl. Phys.* **46**, 6568–6572 (2007).
 - ⁴⁴G. Yang and Y. Li, "Analysis and control of thermal and structural deformation of projection optics for 22-nm EUV lithography," in *Extreme Ultraviolet (EUV) Lithography III*, Vol. 8322 (International Society for Optics and Photonics, 2012) p. 83222V.
 - ⁴⁵R. M. van der Horst, J. Beckers, E. A. Osorio, D. I. Astakhov, W. J. Goedheer, C. J. Lee, V. V. Ivanov, V. M. Krivtsum, K. N. Koshelev, D. V. Lopaev, F. Bijkerk, and V. Y. Banine, "Exploring the electron density in plasma induced by EUV radiation: I. Experimental study in hydrogen," *J. Phys. D: Appl. Phys.* **49**, 145203 (2016).
 - ⁴⁶R. A. Meijer, A. S. Stodolna, K. S. E. Eikema, and S. Witte, "High-energy Nd:YAG laser system with arbitrary sub-nanosecond pulse shaping capability," *Opt. Lett.* **42**, 2758–2761 (2017).
 - ⁴⁷D. Kurilovich, A. L. Klein, F. Torretti, A. Lassise, R. Hoekstra, W. Ubachs, H. Gelderblom, and O. O. Versolato, "Plasma propulsion of a metallic microdroplet and its deformation upon laser impact," *Phys. Rev. Appl.* **6**, 014018 (2016).
 - ⁴⁸D. Kurilovich, M. M. Basko, D. A. Kim, F. Torretti, R. Schupp, J. C. Visschers, J. Scheers, R. Hoekstra, W. Ubachs, and O. O. Versolato, "Power-law scaling of plasma pressure on laser-ablated tin microdroplets," *Phys. Plasmas* **25**, 012709 (2018).
 - ⁴⁹B. Liu, D. Kurilovich, H. Gelderblom, and O. O. Versolato, "Mass loss from a stretching semitransparent sheet of liquid tin," *Phys. Rev. Appl.* **13**, 024035 (2020).
 - ⁵⁰B. Liu, R. A. Meijer, J. Hernandez-Rueda, D. Kurilovich, Z. Mazzotta, S. Witte, and O. O. Versolato, "Laser-induced vaporization of a stretching sheet of liquid tin," *J. Appl. Phys.* **129**, 053302 (2021).
 - ⁵¹R. Schupp, L. Behnke, Z. Bouza, Z. Mazzotta, Y. Mostafa, A. Lassise, L. Poirier, J. Sheil, M. Bayraktar, W. Ubachs, R. Hoekstra, and O. O. Versolato, "Characterization of angularly resolved EUV emission from 2- μ m-wavelength laser-driven Sn plasmas using preformed liquid disk targets," *J. Phys. D: Appl. Phys.* **54**, 365103 (2021).
 - ⁵²S. J. Goh, H. J. M. Bastiaens, B. Vratzov, Q. Huang, F. Bijkerk, and K. J. Boller, "Fabrication and characterization of free-standing, high-line-density transmission gratings for the vacuum UV to soft X-ray range," *Opt. Express* **23**, 4421–4434 (2015).
 - ⁵³M. Bayraktar, H. M. J. Bastiaens, C. Bruineman, B. Vratzov, and F. Bijkerk, "Broadband transmission grating spectrometer for measuring the emission spectrum of EUV sources," *NEVAC blad* **54**, 14–19 (2016).
 - ⁵⁴B. Henke, E. Gullikson, and J. Davis, "X-ray interactions: Photoabsorption, scattering, transmission, and reflection at E = 50–30,000 eV, Z = 1–92," *At. Data Nucl. Data Tables* **54**, 181–342 (1993).
 - ⁵⁵T. A. Johnson, R. Soufli, E. M. Gullikson, and M. Clift, "Zirconium and niobium transmission data at wavelengths from 11–16 nm and 200–1200 nm," in *Optical Constants of Materials for UV to X-Ray Wavelengths*, Vol. 5538, edited by R. Soufli and J. F. Seely, International Society for Optics and Photonics (SPIE, 2004) pp. 119 – 124.
 - ⁵⁶A. Joseph, M. H. Modi, A. Singh, R. K. Gupta, and G. S. Lodha, "Analysis of soft x-ray/VUV transmission characteristics of Si and Al filters," in *AIP Conference Proceedings*, Vol. 1512 (American Institute of Physics, 2013) pp. 498–499.
 - ⁵⁷F. R. Powell, P. W. Vedder, J. F. Lindblom, and S. F. Powell, "Thin film filter performance for extreme ultraviolet and x-ray applications," *Opt. Eng.* **29**, 614 – 624 (1990).
 - ⁵⁸greateyes GmbH, "Scientific Full-frame CCD Cameras for VUV, EUV, X-Ray Imaging and Spectroscopy," (2017).
 - ⁵⁹J. Heymes, M. Soman, G. Randall, A. Gottwald, A. Harris, A. Kelt, I. Moody, X. Meng, and A. D. Holland, "Comparison of back-thinned detector ultraviolet quantum efficiency for two commercially available passivation treatments," *IEEE Trans. Nucl. Sci.* **67**, 1962–1967 (2020).
 - ⁶⁰J. R. Janesick, *Scientific charge-coupled devices*, Vol. 83 (SPIE press, 2001).
 - ⁶¹J. Heymes, M. Soman, T. Buggey, C. Crews, G. Randall, A. Gottwald, A. Harris, A. Kelt, U. Kroth, I. Moody, X. Meng, O. Ogor, and A. Holland, "Calibrating Teledyne-e2v's ultraviolet image sensor quantum efficiency processes," in *X-Ray, Optical, and Infrared Detectors for Astronomy IX*, Vol. 11454, edited by A. D. Holland and J. Beletic, International Society for Optics and Photonics (SPIE, 2020) pp. 263 – 273.
 - ⁶²R. A. Stern, L. Shing, and M. M. Blouke, "Quantum efficiency measurements and modeling of ion-implanted, laser-annealed charge-coupled devices: x-ray, extreme-ultraviolet, ultraviolet, and optical data," *Appl. Opt.* **33**, 2521–2533 (1994).
 - ⁶³L. Poletto, A. Boscolo, and G. Tondello, "Characterization of a charge-coupled-device detector in the 1100–0.14-nm (1-eV to 9-keV) spectral region," *Appl. Opt.* **38**, 29–36 (1999).
 - ⁶⁴H. Garnir and P.-H. Lefebvre, "Quantum efficiency of back-illuminated CCD detectors in the VUV region (30–200nm)," *Nucl. Instrum. Methods Phys. Res. B: Beam Interact. Mater. At.* **235**, 530–534 (2005).

